

Foldamer-Based Ultraparameable and Highly Selective Artificial Water Channels that Exclude Protons

Arundhati Roy,^{1,2‡} Jie Shen,^{1,‡} Himanshu Joshi,³ Woochul Song,⁴ Yu-Ming Tu,⁴ Ratul Chowdhury,⁵ Ruijuan Ye,¹ Ning Li,² Changliang Ren,² Manish Kumar,⁶ Aleksei Aksimentiev,³ and Huaqiang Zeng^{1,7*}

The outstanding capacity of aquaporins (AQPs) for mediating highly selective superfast water transport¹⁻⁷ has inspired recent development of supramolecular monovalent ion-excluding artificial water channels (AWCs). AWC-based bioinspired membranes are proposed for desalination, water purification, and other separations applications⁸⁻¹⁸. While some recent progress has been made in synthesizing AWCs that approach the water permeability and ion selectivity of AQPs, a hallmark feature of AQPs – high water transport while excluding protons has not been reproduced. We report on a class of biomimetic, helically folded pore-forming polymeric foldamers, that can serve as long sought-after highly selective ultrafast water-conducting channels exceeding those of AQPs (1.1×10^{10} H₂O molecules/s for AQP1⁷), with high water over monovalent ion transport selectivity ($\sim 10^8$ water molecules over Cl⁻ ion) conferred by the modularly tunable hydrophobicity of the interior pore surface. The best-performing AWC reported here delivers water transport at an exceptionally high rate, 2.5 times that of AQP1, while concurrently rejecting salts (NaCl and KCl) and even protons.

Drawing on Nature for inspiration, biomimicry has provided rich and effective technological solutions to a range of complex problems¹⁹. One challenging line of inquiry in biomimicry is the extent to which man-made materials can mimic Nature or even go beyond the boundaries seen in Nature at the macro and nanoscales. At the molecular level, biological channels play indispensable roles in myriad cellular processes via precisely controlled directional flows of cognate species (including water¹⁻⁷, potassium²⁰, sodium²¹, calcium²², chloride²³, and protons²⁴). These precisely controlled flows occur through narrow, often water-filled, membrane-spanning pores. Nevertheless, the two highly integrated quintessential features collectively seen in many natural membrane channels – high selectivity that is seamlessly integrated with high permeation rate – are exceedingly difficult to replicate in artificially developed membrane materials¹² and more specifically artificial channels and carriers. In fact, despite numerous advances made over the past four decades^{15-18,25-44}, no artificial channels or membranes have reached the performance in transmembrane transport of ions, protons or water molecules by biological channels such as the KcsA potassium channel and AQPs. The unique ability of AQPs to exclude protons while transporting water decouples water transport from maintenance of transmembrane proton gradients⁴⁵ has not been previously reproduced in artificial channels or engineered biological channels. Through a minimalist biomimetic approach, we have for the first time succeeded in outperforming AQP1¹⁻⁷ in water transport rate while concurrently retaining high rejection of both salts (NaCl and KCl) and protons.

The outstanding water over ion transport performance of AQP1 ($\sim 1.1 \times 10^{10}$ H₂O/s⁷ while excluding all ions), estimated at $>10^9$ water molecules over monovalent ions⁴⁶, has inspired the development of AQP-based biomimetic membranes for industrial and municipal desalting and water purification applications⁸⁻¹⁸. Protein-based

membranes, however, are expected to have a high production cost and face perceived challenges with scale up and stability for industrial uses¹¹. These challenges may limit their widespread applications in novel membrane technologies for water purification and other applications including blue energy production, organic solvent nanofiltration and organic solvent reverse osmosis¹⁸. Mimicking the functions of AQPs for enabling a wider range of molecular separations applications, bioinspired supramolecular AWCs have emerged as promising materials.²⁵⁻³⁴ Yet, concurrently attaining high single-channel water permeability and high transport selectivity has proven to be challenging. Indeed, among all hitherto reported AWCs with high selectivity²⁵⁻³³, only very recently were self-assembled AWCs reported to reject salts, and transport water at a rate of 3.0×10^9 H₂O molecules/s^{31,33}, which is $\sim 27\%$ that of AQP1. Carbon nanotube porins (CNTPs) with an internal pore diameter of 4.7 Å exhibit a water conduction rate 2.1 times that of AQP1³⁴. However, CNTPs also conduct Na⁺, K⁺ and protons^{34,41}.

Molecular design principles and considerations for AWCs

In this work, we aim to mimic the water transport function of AQPs using a set of selectivity principles and structural motif not found in AQPs. We speculated that a large hollow tubular cavity, possessing a pore diameter much larger than a water molecule (2.5 Å) but still smaller than a Na⁺ ion with its first hydration shell (~ 9 Å, Supplementary Fig. 1a), might be needed in order to compete with AQPs. More precisely, we wanted to investigate if water transport that does not strictly adhere to the single-file water arrangement in AQP1 and other channels^{32-33,34} might be able to enable water transport rates higher than AQP1.

We attain high salt rejection by these large pores by decorating the interior pore surface with functional groups, which are “incompetent”

¹ Department of Chemistry, College of Science, Hainan University, Haikou, Hainan 570228, China. ² NanoBio Lab, 31 Biopolis Way, The Nanos, Singapore. ³ Department of Physics and Beckman Institute for Advanced Science and Technology, University of Illinois at Urbana-Champaign, Urbana, IL, USA. ⁴ Department of Chemical Engineering, The University of Texas at Austin, Austin, TX, USA. ⁵ Department of Chemical Engineering, The Pennsylvania State University, PA, USA. ⁶ Department of Civil, Architectural and Environmental Engineering, The University of Texas at Austin, TX, USA. ⁷ Institute of Advanced Synthesis, Northwestern Polytechnical University, Xi'an, Shaanxi 710072, China

[‡] These authors contributed equally to this work. *Corresponding author. Email: hqzeng@nwpu.edu.cn (H.Z.)

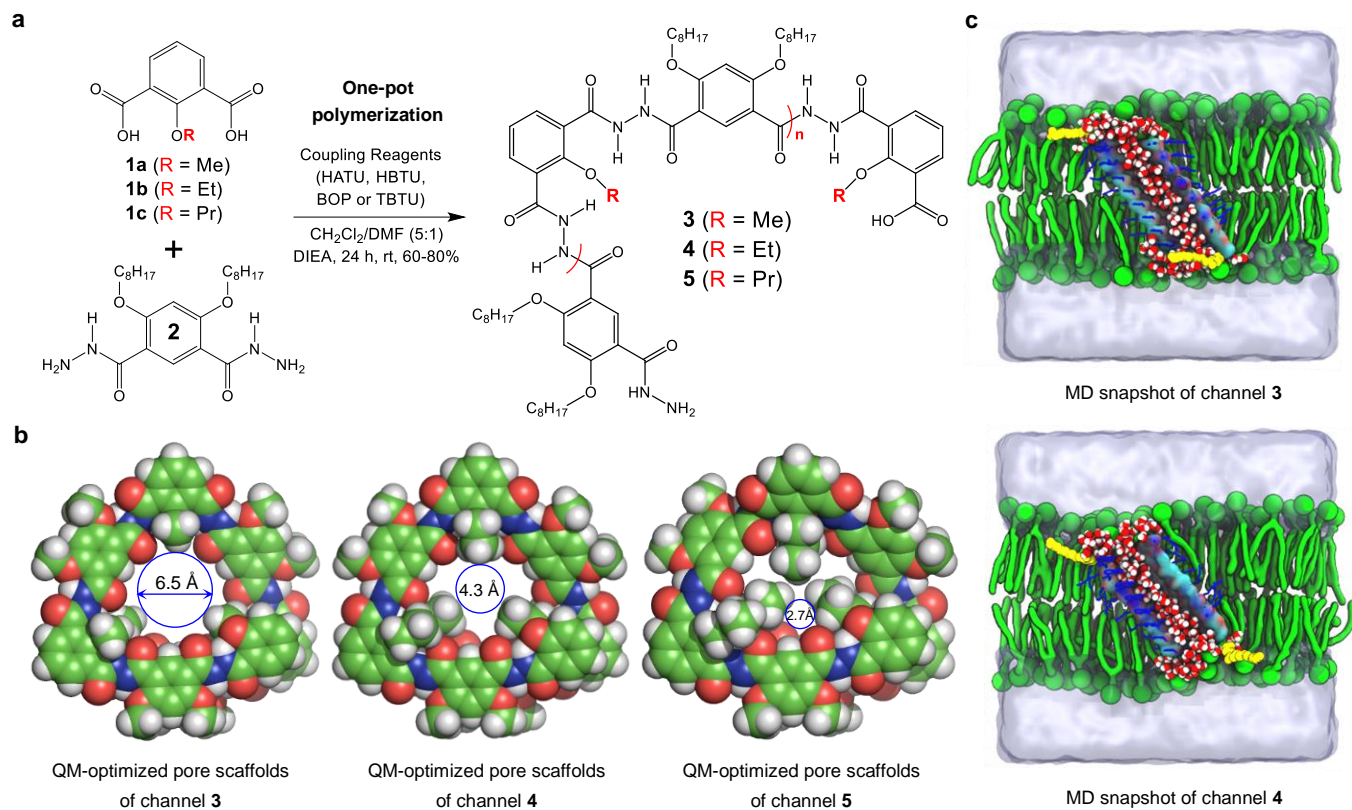


Fig. 1 | Molecular design and synthetic construction of foldamer-derived polymer-based synthetic water channels. **a**, Chemical structures of artificial water channels **3** – **5**, which have inwardly facing methyl- (**3**), ethyl- (**4**), or isopropyl- (**5**) aliphatic groups for tuning the inner-pore size and hydrophobicity, respectively. **b**, QM-optimized backbone scaffolds of **3** – **5**, illustrating excellent structural correspondence to the crystallographic structures of methyl- and ethyl- containing trimeric repeating units (See **6a** and **6b** in Supplementary Fig. 1b for details). **c**, Cross-sections of MD snapshots of water-filled lipid anchor-containing channels **3** and **4**, each containing 26 units of **1** and 25 units of **2** and having a height of 2.9 nm, in POPC membrane. The system is solvated in 1 M NaCl, with the volume occupied by the electrolyte solution represented as semi-transparent surfaces. POPC = (1-palmitoyl-2-oleoyl-*sn*-glycero-3-phosphatidyl choline).

in replacing ion-coordinated water molecules, thereby increasing the barrier to ion entry and passage through the channels⁴⁰. The overall strategy implemented here further involved use of aliphatic chains to render the cavity hydrophobic. Differing from π -electron rich hydrophobicity in CNTs that could interact with cations⁴⁷, such “aliphatic hydrophobicity” conferred by the essentially non-polar C-H bonds provides a slightly positive electrostatic surface⁴⁰ that excludes cations. Although the aliphatic hydrophobic surface has been shown to interact favourably with anions^{48,49}, a sufficiently small hydrophobic cavity (e.g. 4.3 Å in **4**) may block anion transport. Moreover, we focused on designs where one-dimensional H-bonded water chains cannot be formed continuously inside the pores. This was achieved by obstructing continuous proton transfer to adjacent water molecules, thereby blocking proton transport. In doing so, fluctuation of hydrophobic groups disrupts the water wire, distinct from that in Asparagine Proline Alanine (NPA), centrally located in AQPs⁵⁰. This work also addresses the question of whether continuously formed H-bonded water chains (seen in CNTPs³⁴ and other channels^{32,33}) are essential for rapid water transport.

Molecular design and structural features of AWCs 3-5

We recently reported polymeric channels **3** (Fig. 1a) derived from an H-bond-rigidified foldamer-based hydrazide backbone⁴⁰. Arising from hydrophobic methyl groups, the well-separated interior O-atoms

(cavity of ~ 6.5 Å) can't form a convergent cation-binding pocket (Fig. 1b) but allows for anion transport. Considering these design principles, the interior methyl groups (Me) in **3** were replaced by ethyl (Et) or propyl (Pr) groups to afford two new classes of polymer channels **4** and **5**, having smaller hydrophobic cavities to minimize anion-specific interactions.

Quantum mechanics (QM) calculations of pore scaffolds at the ω B97X/6-31G(d) level were adopted to understand the structural features of **3** – **5**. The central fragments of QM-computed pore of **3** and **4** (Fig. 1b) are nearly-identical to crystal structures of trimer molecules **6a** and **6b**, respectively, indicating high reliability of computed pore sizes of ≥ 6.5 Å for **3**, ≥ 4.3 Å for **4** and three segregated pores of ~ 2.7 Å for **5**. Based on these QM-derived structures, we built 2.9 nm long channel structures **3** – **5**, each having 26 units of **1** and 25 units of **2**. All-atom molecular dynamics (MD) simulation^{2,4} was conducted by embedding channels in POPC lipid membrane surrounded by 1M NaCl to provide further structural insights. As expected, both **3** and **4** enclose a water-filled sizable cavity of > 4 Å (Fig. 1c and Supplementary Fig. 1c), whereas the cavity of **5** is mostly blocked by the Pr groups (Supplementary Fig. 1c).

High water permeability of AWCs 3-5

Following a recently reported one-pot polymerization protocol⁴⁰, twelve AWCs (**3** – **5**) were readily made from repeating units **1** and **2**

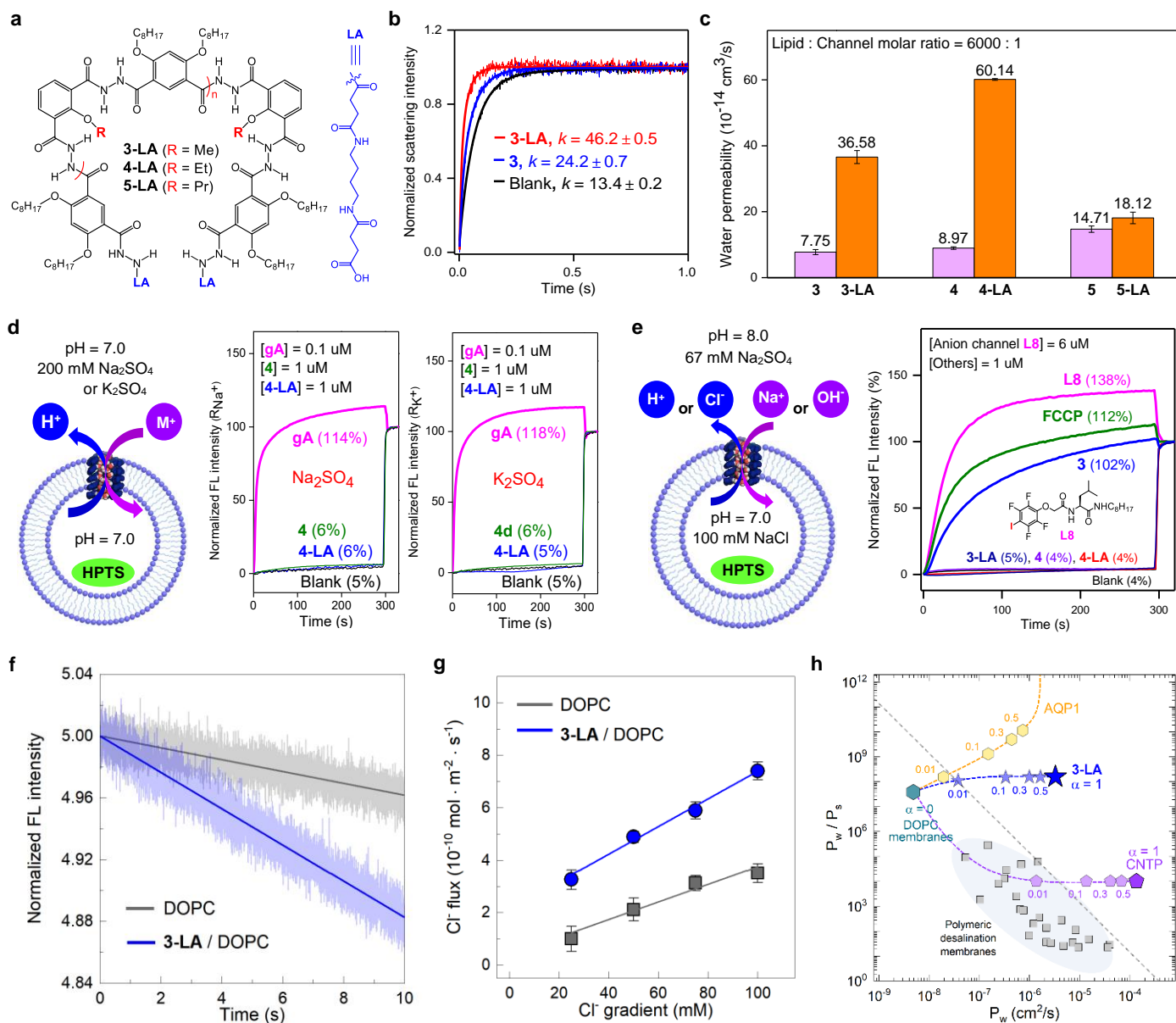


Fig. 2 | Selective water permeation through foldamer-based polymeric AWCs. **a**, Chemical structures of lipid anchor (LA)-modified AWCs. **b**, Representative stopped-flow light scattering traces of **3** and **3-LA** reconstituted DOPC vesicles under the inwardly directed osmotic gradients. **c**, Single channel permeability of channels before and after LA modification. **d** and **e**, Schematic illustrations of HPTS-based fluorescence assays, demonstrating high rejection of (**d**) cations (Na^+ or K^+) and (**e**) anion (Cl^-) and proton through the channels. **f**, Stopped-flow fluorescence traces of **3-LA** reconstituted DOPC vesicles, encapsulating lucigenin dyes for sensing Cl^- permeation that is driven by inwardly directed Cl^- concentration gradients (20 mM). **g**, Plots of Cl^- permeation flux as a function of Cl^- concentration gradients for both DOPC and **3-LA** reconstituted DOPC membranes. **h**, Comparison of water-to-salt permselectivity of **3-LA** to the values of several representative water channels and current polymeric desalination membranes. Intrinsic water-to-salt selectivity (P_w/P_s) vs water permeability (P_w , cm^2/s) plot. P_w/P_s vs P_w values for **3-LA** reconstituted biomimetic membranes in a DOPC matrix, which were compared with other representative water channels, AQP1 and CNTPs with pore diameter of ~ 0.47 nm^{13,34}. The α values in the plot indicate the fractional volume of the biomimetic membranes occupied by water channels (e.g., $\alpha = 0.5$ represents the membranes of which the half volume is composed of the channels). Dashed line is the current polymer desalination membranes' permeability-selectivity upper bound limit^{10,12}. Data in **c**, **f**) and **g**) are the average of three independent measurements with error bars representing the standard deviations.

and the four coupling reagents (HATU, HBTU, BOP and TBTU, see Fig. 1a and Supplementary Fig. 2 and Supplementary Tables 1-3 for details), with GPC-derived molecular weights (M_n) of 11.6 – 27.3 kDa and nanotube lengths of 2.1 – 5.1 nm.

Single channel water permeability (P_{sc} in cm^3/s) was investigated by a stopped-flow method²⁵⁻³⁴, using 0.3 M sucrose as the draw solution.

To facilitate quick identification of effective AWCs, 100% channel membrane insertion efficiency was assumed for all channels, which turns out to be a valid one as the actual channel insertion efficiencies were found to be near-identical among **3** – **5** under the identical conditions (see latter discussion). By varying the lipid to channel molar ratios (mLCR) from 1500:1 to 9000:1, 3.0 nm long channel **3**

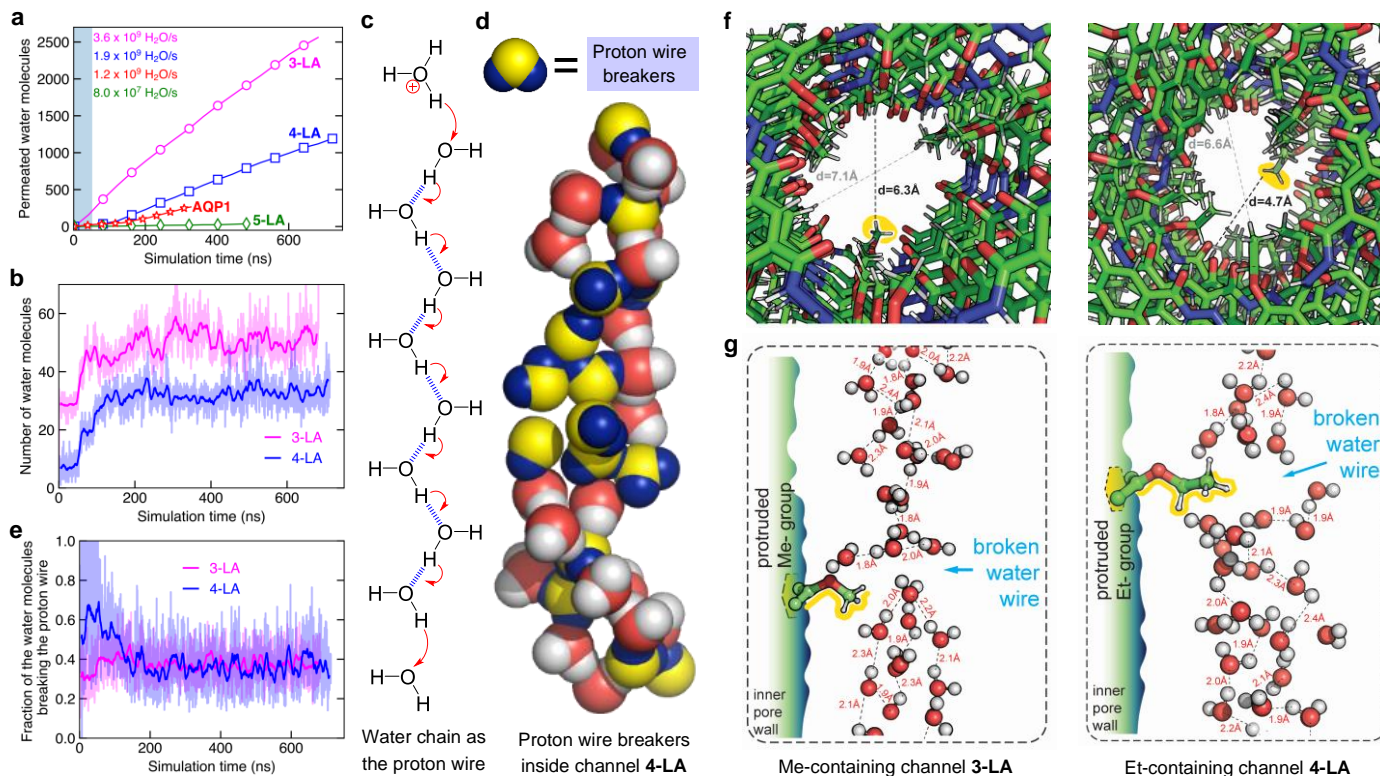


Fig. 3 | MD simulations of water transport and the mechanism of proton rejection by proton wire breakers created due to the presence of fluctuating alkyl groups. **a**, Number of water molecules observed to pass through LA-containing **3 - 5** and AQP1 in equilibrium MD simulations. The channel structure was harmonically restrained for the first 50 ns. **b**, Number of water molecules inside the pores of channels **3-LA** and **4-LA**. **c**, Illustration of proton transport through an ideal proton wire via the Grotthuss mechanism. **d**, Irregularly H-bonded water molecules, serving as proton wire breakers to block proton transport via the Grotthuss mechanism. **e**, Fractions of proton wire breakers over all water molecules inside **3-LA** and **4-LA**. **f**, Inward protrusions of Me and Et groups transiently reduce local cross section of channels **3-LA** and **4-LA**. **g**, Breakage of proton water wire caused by protrusion of Me (left) and Et (right) groups.

synthesized using HATU was found to elicit the maximum permeability at mLCR of 6000:1 (Supplementary Fig. 3 and Supplementary Table 4). Keeping the mLCR fixed at 6000:1, single channel permeability (P_{sc}) values appear to plateau at a channel height of 3.0 nm ($7.75 \pm 0.76 \times 10^{-14}$ cm³/s) among series **3**, of 3.1 nm ($8.97 \pm 0.76 \times 10^{-14}$ cm³/s) among series **4**, and of 2.1 nm ($14.72 \pm 0.97 \times 10^{-14}$ cm³/s) among series **5** (Supplementary Table 5). These values translate into water transport rates of $\sim 10^9$ H₂O molecules/s.

Ultrapermability of lipid anchor-modified 4-LA

We surmised that **3** and **4** likely could transport water molecules much faster than $\sim 10^9$ H₂O molecules/s because their pore sizes are much larger than a water molecule. Channels **3** and **4** lack hydrophilic end groups for aligning channels to span lipid bilayers seen in other water channels, leading us to hypothesize that many channel orientations not conducive for water transport may exist. To examine this surmise, carboxylic acid-based “lipid anchors” (LAs, Fig. 2a) were attached at both termini of the most active channels among series **3**, **4** and **5** to produce **3-LA**, **4-LA** and **5-LA** and evaluate their water transport activity.

Compared to **3** free of lipid anchors, water conduction of **3-LA** was greatly improved (Fig. 2b), and its P_{sc} value averaged over three runs was determined to be $36.58 \pm 1.97 \times 10^{-14}$ cm³/s at a mLCR of 6000:1 (Fig. 2c). Similarly, P_{sc} values of **4-LA** and **5-LA** were increased to $60.14 \pm 0.17 \times 10^{-14}$ cm³/s and $18.12 \pm 1.76 \times 10^{-14}$ cm³/s, respectively.

After corrections using channel insertion efficiencies of 66%, 75%, and 75% for **3-LA**, **4-LA** and **5-LA** (Supplementary Fig. 4 and Supplementary Table 6), their respective water conduction rates were determined to be $1.6 \pm 0.06 \times 10^{10}$, $2.7 \pm 0.005 \times 10^{10}$ and $0.8 \pm 0.05 \times 10^{10}$ H₂O/s. Particularly, the **4-LA**-mediated ultrafast water conduction of 2.7×10^{10} H₂O/s represents a large improvement of 145% over that of AQP1 (1.1×10^{10} H₂O/s)⁷ and is even higher than that of CNTPs (2.3×10^{10} H₂O/s)³⁴ at pH 7.

The water transport activation energy values (E_a) for DOPC membrane only, **3-LA**, **4-LA** and **5-LA** were determined to be 12.3 ± 1.3 , 8.7 ± 1.2 , 8.3 ± 0.9 and 11.5 ± 1.2 Kcal/mol, respectively (Supplementary Fig. 5). Consistent with recent observations by us^{32,33} and others^{4,33}, E_a value for more permeable **4-LA**, while lower than for a pure lipid membrane, turns out to be larger than that of less permeable AQP1 (~ 5 Kcal/mol)⁵. This suggests that the low E_a seen in AQP channels^{7,51} may not be a requirement for all highly permeable channels, particularly when the transport is not strictly single water-wire mediated. Pohl et al has recently shown that reduced friction (i.e., lower number of H-bonds water may form with channel-lining residues, less friction) could increase hundred-fold water permeability.⁷ We have also shown that three factors (i.e., pore volume, friction and deviation from optimum H-bonded water chain structure) collectively yet decisively contribute to 15-fold difference in single-channel permeability.³³ Therefore, although **3-LA** and **4-LA** have similar E_a (8.7 ± 1.2 vs 8.3 ± 0.9 Kcal/mol) larger than ~ 5 Kcal/mol for AQPs,

we speculate that it is the hydrophobic alkyl groups that generate a lower friction pore to generate higher water transport rates than AQPs. In addition, ethyl-containing **4-LA** may have a more hydrophobic pore that experience smaller resistance, resulting in faster transport rate than **3-LA**. Further, given that E_a is a measure of the enthalpic energy barrier for transport in narrow channels but entropic barriers could also be important, we suspect that entropy may be part of the answer to why **3-LA** and **4-LA** exhibit faster water transport rates than AQPs while having higher E_a values.

High rejection of salts and protons by **4-LA**

Another indispensable criterion of being an ideal AWC is the ability to reject salts (KCl and NaCl) and, ideally, protons. At an mLCR of 6000:1, the measured P_f values for **4-LA** were 117.5 ± 4.5 , 121.5 ± 3.8 and 124.7 ± 0.3 cm/s for sucrose, NaCl and KCl, respectively. The corresponding reflection coefficients, defined as the ratio of P_f values, are 1.03 ± 0.01 for $P_f(\text{NaCl})/P_f(\text{sucrose})$ and 1.06 ± 0.006 for $P_f(\text{KCl})/P_f(\text{sucrose})$, suggesting that **4-LA** achieves high rejection of NaCl and KCl^{28,32,33}. These approximate values indicating salt rejection can be corroborated by the low reflection coefficients of 0.53 ± 0.02 and 0.07 ± 0.001 for cation channel gramicidin A (gA), which is highly permeable to both Na^+ and K^+ ions, respectively.

High rejection of Na^+ and K^+ was validated further using LUVs (large unilamellar vesicles of about 120 nm in diameter) based assays, with entrapped pH-sensitive HPTS dye (Fig. 2d). Unsurprisingly, **4** and **4-LA** at 1 μM both are completely inactive towards both K^+ and Na^+ ions, whereas dimeric gA, at channel concentration 20 times smaller (0.1 μM), transports both Na^+ (114%) and K^+ (118%) at high rates. The presence of **4-LA** in the membrane can be established by the measured membrane insertion efficiency of $\geq 75\%$ under the identical conditions (Supplementary Fig. 7). Additional testing similarly reveals high cation rejections by **3**, **3-LA**, **5** and **5-LA** (Supplementary Fig. 8a), demonstrating that a pore as large as 6.5 Å in **3** can effectively prevent both Na^+ and K^+ from entering it, along with the smaller mostly hydrophobic pores **4** and **5**.

High rejection of Cl^- and protons can also be confirmed using the LUV scheme in Fig. 2e. Specifically, when compared to a self-assembled chloride channel (**F8**)₆⁵² that induces a high chloride transport activity of 138%, and to the proton carrier FCCP that induces a high proton transport activity of 112%, both the anion and proton transport rates of **3-LA**, **4**, **4-LA** (Fig. 2e), **5** and **5-LA** (Supplementary Fig. 8b) were non-detectable. A large difference in Cl^- transport between **3** and **3-LA** can be ascribed to the fact that the lipid anchor in **3-LA** contains a carboxylic acid group, ionizing to become a negatively charged carboxylate anion at pH 7. These negative charges at the channel's two ends may reduce the chance of anion entering the transmembrane pore, attenuating otherwise high anion transport activity of **3**⁴⁰. Additionally, a conservative estimate indicates the **4-LA**-induced proton transport rate to be < 0.01 proton/s (Supplementary Fig. 9 and the corresponding supplementary discussions) at pH 7. This value is in great accord with the quantitative proton permeation rate of < 0.1 proton/s measured using stopped-flow fluorescence spectroscopy (Supplementary Figs. 10-12).

High rejection of Cl^- also can be established by using a chloride-sensitive SPQ dye (Supplementary Fig. 8c). Except for **3**, channels **3-LA**, **4**, **4-LA**, **5** and **5-LA** all caused quenching of SPQ dye undifferentiated from the background, whereas (**F8**)₆ displayed 45% fluorescence quenching. Thus, results of these LUV-based assays provide evidence of high rejection of both salts and protons by

ultrapermeable **4-LA** and by superpermeable **3-LA**, **4**, **5** and **5-LA**.

To evaluate the molecular separation property of the channels for desalination applications, monovalent ion permeability of **3-LA** was measured, and its water-to-salt permselectivity compared to the values of the other representative membrane materials^{10,12,13,34}. Cl^- ion permeability was measured using stopped-flow fluorescence analysis, with lucigenin dyes as molecular sensing probes (Fig. 2f), as demonstrated in a recent study³¹. We chose to use Cl^- transport to provide a conservative value because Cl^- sensitive fluorescent dyes were found to be more sensitive sensors in a recent study³¹.

Quantitative Cl^- permeation through DOPC membrane in absence and presence of **3-LA** were measured at several different inwardly directly concentration gradients (Fig. 2g and Supplementary Fig. 13a). Based on the channel density in membrane, the single channel chloride ion permeability was calculated to be $9.5 \pm 7.5 \times 10^{-21}$ cm³/s for **3-LA**. As shown in Fig. 2h, the **3-LA**'s water-to-salt permselectivity was calculated as $1.6 \pm 2.5 \times 10^8$, which overcomes the current desalination membranes' permeability-selective trade-off trendline^{10,12} by a factor of $\sim 10^3$, demonstrating good potential for using foldamer-derived AWCs in desalination membrane development.

MD simulation of water transport and proton rejection mechanism

Equilibrium MD simulations of **LA**-containing **3** - **5** (2.9 nm long, each having 26 units of **1** and 25 units of **2**), and of AQP1 embedded in a solvated POPC membrane (Fig. 1c and Supplementary Fig. 14) yielded the water permeation rates of 3.6, 1.9, 1.2 and 0.08×10^9 H₂O/s for **3-LA**, **4-LA**, AQP1 and **5-LA** (Fig. 3a and Supplementary Movies 1-3), respectively. Although these values do not exactly match the experimental values, they do show a comparable trend, *i.e.*, both **3-LA** and **4-LA** are more permeable to water than AQP1, with **5-LA** being the least permeable. After their nonhydrogen atoms were no longer restrained to the coordinates of the initial idealized model, **3-LA** and **4-LA** were observed to accommodate considerably more water molecules (Fig. 3b), giving rise to considerable increases in water flux. Interestingly, the **LA** groups were observed to flop around the channel's termini, occasionally stacking at the rim of the channel (Supplementary Movies 1-3). While we do see a small defect in the structure of **3-LA** and also see some water molecules transiently attaching to channel's outer surface, we do not see any transmembrane water permeation through the defects or along the outer surface. The fact that experimental water transport rates between structurally similar **4** and **4-LA** differ by > 6 -fold clearly suggest water moving around the channel to pass through the membrane won't be primarily responsible for the high water transport rate seen in **4-LA**. Thus, water transport outside the central channels is likely negligible. Meanwhile, we found **5-LA** to barely contain or conduct any water. We attribute this qualitative disagreement with experiment to the initial structural model of the channel, which may not truly represent its relaxed configuration in the membrane, and to the simulation time scale, which was too short for the channel to find its equilibrium configuration.

At first sight, the many water molecules within these channels (~ 48 inside **3-LA** and ~ 33 inside **4-LA**, Fig. 3b) should readily facilitate proton transport, which nevertheless is not observed experimentally. According to the Grothuss mechanism, a water chain forms a proton wire for proton transport when every water molecule of the chain forms two H-bonds with its neighbors, one using its O atom and another one using its H atom (Fig. 3c). Conversely, water molecules forming no or

just one H-bond, or forming two H-bonds both solely via only O or only H atoms can be described as the proton wire breakers, blocking proton transport through a water chain (Fig. 3d). The latter is observed in AQPs, where water molecule(s) in the approximate center of the channel form up to two H-bonds with the adjacent water molecules using only H atoms, because the O atoms of these central water molecules are H-bonded by the NPA motif⁵⁰. Thus, a proton is not able to hop on or off these water molecule. Nevertheless, as suggested by few, we do acknowledge that the electrostatic effect of positively charged residues lining the pore may play an important and perhaps even a predominant role in inhibiting proton passage through AQPs⁴⁵. In this work, we find that the molecular architecture of **3-LA** and **4-LA** creates several such proton wire breakers that prevent proton hopping through the water molecules, and that these proton wire breakers alone seem to be sufficient to achieve a high level of proton rejection. On average, about 36% of water molecules in **3-LA** and **4-LA** are found to satisfy the criteria of being proton wire breakers (Fig. 3e). One statistically meaningful snapshot in Fig. 3d illustrates 15 proton wire breakers and 20 regularly H-bonded water molecules in **4-LA**. The Supplementary Fig. 17 highlights a snapshot of **3-LA**, having 26 proton wire breakers and 27 regularly H-bonded water molecules. The presence of these proton wire breakers reduces the average length of single file H-bonded water chain from 29 Å to 12.5 ± 1.5 Å for **3-LA** and to 10.6 ± 0.4 Å for **4-LA**.

To gain further insights into proton rejection mechanism in **3-LA** and **4-LA**, we investigated the spatio-temporal dynamics of the intra-water hydrogen bonded networks. For our analysis, we split the channel's volume into seven disk-like zone. The MD trajectories of the channels were analyzed to quantify the number of breaks in the water chain and effective pore size in each of the zones using PoreAnalyzer⁵³. Out of 500 MD frames (Supplementary Fig. 18), 67% and 79% have at least one break in the water wire network for **3-LA** (an average of 1.65 breaks/channel) and **4-LA** (an average of 1.86 breaks/channel), respectively. These indicate that for more than two-thirds of the simulation time, there exists no route for protons to permeate through these channels by hopping from one H-bonded water molecule to another via short-lived hydronium ion (H_3O^+) formation. For the remaining 1/3 of MD frames, it is possible that they may be undergoing transitions from one broken proton wire conformation to another, assuming that these transitions may occur at a rate slower than the rate at which the MD frames were collected. The inward-facing Me and Et groups of the Me-containing **3-LA** and Et-containing **4-LA** were found to protrude by up to 1.84 Å and 2.75 Å, respectively, from the pore wall into the water-filled pore (Fig. 3f). These protrusions not only cause a fluctuation of the local pore size from 5.2 Å to 7.1 Å for **3-LA**, and from 4.6 Å to 6.7 Å for **4-LA**, but also a break in the water chain (Fig. 3g). For **3-LA**, 86% of the disks with an average 1.74 Å Me-group protrusion length shows a break in water chain. In **4-LA**, 91% disks with average Et-protrusion length of 2.64 Å is associated with a break (Supplementary Fig. 18). This proton-blocking mechanism where proton wire breaks occur at various locations along the channel by fluctuating hydrophobic interior groups is unprecedented, and works synergistically with the many proton wire breakers to endow channels **3-LA** and **4-LA** with high degree of proton exclusion.

Lastly, to estimate the E_a for water entry into the channels, we computed the number of H-bonds per water molecule formed between water and channel wall, and among water molecules for all three channels (Table 1 and Supplementary Fig. 19a-c). Taking 5.1 kcal/mol as the H-bond energy obtained from an isolated water dimer and each

Table 1. Computed number of intermolecular H-bonds per water molecule formed among water molecules in the channel, and between water molecule and channel's inner wall^a

	3-LA	4-LA	AQP1
Water-Water	2.0 (± 0.2)	1.9 (± 0.3)	1.6 (± 0.1)
Water-Wall	0.8 (± 0.1)	0.8 (± 0.1)	1.6 (± 0.1)
Total	2.8 (± 0.3)	2.7 (± 0.4)	3.2 (± 0.2)

^a Average values and standard deviations in H-bond were computed for the whole simulation trajectory after excluding the first 50 ns of the simulation where the channels were harmonically restrained (Supplementary Fig. 19a-c).

water forming four H-bonds in bulk water^{54,55}, the activation energies can be estimated to be 6.1, 6.3 and 4.1 kcal/mol for **3-LA**, **4-LA** and AQP1, respectively. These values are consistent with their respective experimental activation energies of 8.7, 8.3 and 5.0 kcal/mol. We have further used the replica-exchange umbrella sampling method to compute the free energy profile of water molecules translocating through **3-LA**, **4-LA**, and AQP1 channels embedded in the POPC lipid

bilayer membrane (Supplementary Fig. 19d). Consistent with the experimentally determined activity energies, both **3-LA** and **4-LA** are found to have a higher barrier (~ 3 kcal/mol) than AQP1 (~ 1 kcal/mol) for water to translocate throughout the pore as seen from potential of mean force (PMF) calculations. Although the barrier and activation energies for water permeation are both higher in **3-LA** and **4-LA** than AQP-1, we do observe more water permeation in these two AWCs than AQP1 in equilibrium simulations. As discussed earlier, this could be due to the wider pore sizes of AWCs as well as the lower number of H-bonds formed between water molecules and the pore-lining functional groups (0.8 H-bond per water molecule for AWCs vs 1.6 H-bonds per water molecule for AQP1, Table 1), making water movement in AWCs more frictionless.

Summary

In summary, we have presented here novel strategies for molecular evolution of foldamer-based ultrapermeable AWCs, derived from a fully H-bonded, helically folded and pore-forming hydrazide backbone. Tuning of interior groups and attachment of lipid-anchors were exploited to enhance water permeability and salt rejection. Exhibiting ultrahigh single-channel water permeability of 2.7×10^{10} H₂O/s, the most permeable channel **4-LA** further possesses high capacity to reject both salts and protons. This is the first nanometer-sized AWC truly emulating the key water transport features of biological water channels. This ultrapermeable artificial aquaporin might have the potential to become the preferred candidate for fabricating next-generation membranes for water purification as well as other challenging nanobiotechnological applications where high water transport but proton and ion exclusion is required. Going beyond the specific designs presented here, we can envision a variety of foldamer-based hydrazide water channels, made up of different types of helicity codons³², having similar intermediate pore sizes as **4-LA**, paralleling or even surpassing the water transport performances of **4-LA**.

Online content

Any methods, additional references, Nature Research reporting summaries, source data, extended data, supplementary information, acknowledgements, peer review information; details of author contributions and competing interests; and statements of data availability are available.

References

- 1 Murata, K. *et al.* Structural determinants of water permeation through aquaporin-1. *Nature* **407**, 599-605 (2000).
- 2 Tajkhorshid, E. *et al.* Control of the Selectivity of the Aquaporin Water Channel Family by Global Orientational Tuning. *Science* **296**, 525-530 (2002).
- 3 Takata, K., Matsuzaki, T. & Tajika, Y. Aquaporins: water channel proteins of the cell membrane. *Progress in histochemistry and cytochemistry* **39**, 1-83 (2004).
- 4 de Groot, B. L. & Grubmüller, H. Water permeation across biological membranes: mechanism and dynamics of aquaporin-1 and GlpF. *Science* **294**, 2353-2357 (2001).
- 5 Agre, P. Aquaporin Water Channels (Nobel Lecture). *Angew. Chem. Int. Ed.* **43**, 4278-4290 (2004).
- 6 Borgnia, M. J., Kozono, D., Calamita, G., Maloney, P. C. & Agre, P. Functional reconstitution and characterization of AqpZ, the E. coli water channel protein. *J. Mol. Biol.* **291**, 1169-1179 (1999).
- 7 Horner, A. *et al.* The mobility of single-file water molecules is governed by the number of H-bonds they may form with channel-lining residues. *Sci. Adv.* **1**, e1400083 (2015).
- 8 Fane, A. G., Wang, R. & Hu, M. X. Synthetic Membranes for Water Purification: Status and Future. *Angew. Chem. Int. Ed.* **54**, 3368-3386 (2015).
- 9 Werber, J. R., Osuji, C. O. & Elimelech, M. Materials for next-generation desalination and water purification membranes. *Nat. Rev. Mater.* **1** (2016).
- 10 Park, H. B., Kamcev, J., Robeson, L. M., Elimelech, M. & Freeman, B. D. Maximizing the right stuff: The trade-off between membrane permeability and selectivity. *Science* **356**, eaab0530 (2017).
- 11 Hélix-Nielsen, C. Biomimetic Membranes as a Technology Platform: Challenges and Opportunities. *Membranes* **8**, 44-59 (2018).
- 12 Werber, J. R. & Elimelech, M. Permselectivity limits of biomimetic desalination membranes. *Sci. Adv.* **4**, eaar8266 (2018).
- 13 Freger, V. Selectivity and polarization in water channel membranes: lessons learned from polymeric membranes and CNTs. *Faraday Discuss.* **209**, 371-388 (2018).
- 14 Wagh, P. & Escobar, I. Biomimetic and bioinspired membranes for water purification: A critical review and future directions. *Environ. Prog. Sustain. Energy* **38** (2019).
- 15 Barboiu, M. & Gilles, A. From Natural to Bioassisted and Biomimetic Artificial Water Channel Systems. *Acc. Chem. Res.* **46**, 2814-2823 (2013).
- 16 Huo, Y. P. & Zeng, H. Q. "Sticky"-Ends-Guided Creation of Functional Hollow Nanopores for Guest Encapsulation and Water Transport. *Acc. Chem. Res.* **49**, 922-930 (2016).
- 17 Gong, B. Artificial water channels: inspiration, progress, and challenges. *Faraday Discuss.* **209**, 415-427 (2018).
- 18 Song, W. & Kumar, M. Artificial water channels: toward and beyond desalination. *Curr. Opin. Chem. Eng.* **25**, 9-17 (2019).
- 19 Bhushan, B. Biomimetics: lessons from nature—an overview. *Phil. Trans. R. Soc. A.* **367**, 1445-1486 (2009).
- 20 Doyle, D. A. *et al.* The structure of the potassium channel: molecular basis of K⁺ conduction and selectivity. *Science (New York, N.Y.)* **280**, 69-77 (1998).
- 21 Yu, F. H. & Catterall, W. A. Overview of the voltage-gated sodium channel family. *Genome Biol.* **4**, 207 (2003).
- 22 Reuter, H. A variety of calcium channels. *Nature* **316**, 391 (1985).
- 23 Dutzler, R., Campbell, E. B. & MacKinnon, R. Gating the Selectivity Filter in CIC Chloride Channels. *Science* **300**, 108-112 (2003).
- 24 Mould, J. A. *et al.* Mechanism for Proton Conduction of the M2 Ion Channel of Influenza A Virus. *J. Biol. Chem.* **275**, 8592-8599 (2000).
- 25 Kaucher, M. S. *et al.* Selective Transport of Water Mediated by Porous Dendritic Dipeptides. *J. Am. Chem. Soc.* **129**, 11698-11699 (2007).
- 26 Zhou, X. B. *et al.* Self-assembling subnanometer pores with unusual mass-transport properties. *Nat. Commun.* **3**, 949 (2012).
- 27 Hu, C. B., Chen, Z. X., Tang, G. F., Hou, J. L. & Li, Z. T. Single-Molecular Artificial Transmembrane Water Channels. *J. Am. Chem. Soc.* **134**, 8384-8387 (2012).
- 28 Licsandru, E. *et al.* Salt-Excluding Artificial Water Channels Exhibiting Enhanced Dipolar Water and Proton Translocation. *J. Am. Chem. Soc.* **138**, 5403-5409 (2016).
- 29 Zhao, H. Q., Sheng, S., Hong, Y. H. & Zeng, H. Q. Proton Gradient-Induced Water Transport Mediated by Water Wires inside Narrow Aquapores of Aquafoldamer Molecules *J. Am. Chem. Soc.* **136**, 14270-14276 (2014).
- 30 Shen, Y.-X. *et al.* Highly permeable artificial water channels that can self-assemble into two-dimensional arrays. *Proc. Natl. Acad. Sci. USA* **112**, 9810-9815 (2015).
- 31 Song, W. *et al.* Artificial water channels enable fast and selective water permeation through water-wire networks. *Nat. Nanotech.* **15**, 73-79 (2020).
- 32 Shen, J. *et al.* Polypyridine-Based Helical Amide Foldamer Channels: Rapid Transport of Water and Protons with High Ion Rejection. *Angew. Chem. Int. Ed.* **59**, DOI: 10.1002/anie.202003512 (2020).
- 33 Shen, J. *et al.* Aquafoldamer-Based Aquaporin-like Synthetic Water Channel. *J. Am. Chem. Soc.* **142**, 10050-10058 (2020).
- 34 Tunuguntla, R. H. *et al.* Enhanced water permeability and tunable ion selectivity in subnanometer carbon nanotube porins. *Science* **357**, 792-796 (2017).
- 35 Gale, P. A., Davis, J. T. & Quesada, R. Anion transport and supramolecular medicinal chemistry. *Chem. Soc. Rev.* **46**, 2497-2519 (2017).
- 36 Sakai, N. & Matile, S. Synthetic Ion Channels. *Langmuir* **29**, 9031-9040 (2013).
- 37 Si, W., Xin, P., Li, Z.-T. & Hou, J.-L. Tubular Unimolecular Transmembrane Channels: Construction Strategy and Transport Activities. *Acc. Chem. Res.* **48**, 1612-1619 (2015).
- 38 Howorka, S. Building membrane nanopores. *Nat. Nanotech.* **12**, 619-630 (2017).
- 39 Zheng, S.-P., Huang, L.-B., Sun, Z. & Barboiu, M. Self-assembled Artificial Ion-Channels toward Natural Selection of Functions. *Angew. Chem. Int. Ed.* **59**, DOI: 10.1002/anie.201915287 (2020).
- 40 Roy, A. *et al.* Polyhydrazide-Based Organic Nanotubes as Efficient and Selective Artificial Iodide Channels. *Angew. Chem. Int. Ed.* **59**, 4806-4813 (2020).
- 41 Tunuguntla, R. H., Allen, F. L., Kim, K., Belliveau, A. & Noy, A. Ultrafast proton transport in sub-1-nm diameter carbon nanotube porins. *Nat. Nanotech.* **11**, 639-644 (2016).
- 42 Ren, C. *et al.* Molecular Swings as Highly Active Ion Transporters. *Angew. Chem. Int. Ed.* **58**, 8034-8038 (2019).
- 43 Zeng, L. Z., Zhang, H., Wang, T. & Li, T. Enhancing K⁺ transport activity and selectivity of synthetic K⁺ channels via electron-donating effects. *Chem. Commun.* **56**, 1211-1214 (2020).
- 44 Chen, F. *et al.* Pyridine/Oxadiazole-Based Helical Foldamer Ion Channels with Exceptionally High K⁺/Na⁺ Selectivity. *Angew. Chem. Int. Ed.* **59**, 1440-1444 (2020).
- 45 de Groot, B., Frigato, T., Helms, V. & Grubmüller, H. The Mechanism of Proton Exclusion in the Aquaporin-1 Water Channel. *J. Mol. Biol.* **333**, 279-293 (2003).
- 46 Pohl, P., Saparov, S. M., Borgnia, M. J. & Agre, P. Highly selective water channel activity measured by voltage clamp: Analysis of planar lipid bilayers reconstituted with purified AqpZ. *Proc. Natl. Acad. Sci. USA* **98**, 9624-9629 (2001).
- 47 Pham, T. A. *et al.* Salt Solutions in Carbon Nanotubes: The Role of Cation- π Interactions. *J. Phys. Chem. C* **120**, 7332-7338 (2016).
- 48 Kim, K. *et al.* Crystal structure and functional characterization of a light-driven chloride pump having an NTQ motif. *Nat. Commun.* **7**, 12677 (2016).
- 49 Ren, C. L. *et al.* Pore-Forming Monopeptides as Exceptionally Active Anion Channels. *J. Am. Chem. Soc.* **140**, 8817-8826 (2018).
- 50 Kosinska Eriksson, U. *et al.* Subangstrom Resolution X-Ray Structure Details Aquaporin-Water Interactions. *Science* **340**, 1346-1349 (2013).
- 51 Horner, A., Siligan, C., Cornean, A. & Pohl, P. Positively charged residues at the channel mouth boost single-file water flow. *Faraday Discuss.* **209**, 55-65 (2018).
- 52 Ren, C. *et al.* A halogen bond-mediated highly active artificial chloride channel with high anticancer activity. *Chem. Sci.* **9**, 4044-4051 (2018).
- 53 Chowdhury, R. *et al.* PoreDesigner for tuning solute selectivity in a robust and highly permeable outer membrane pore. *Nat. Commun.* **9**, 3661 (2018).
- 54 Zhang, C., Wu, J., Galli, G. & Gygi, F. Structural and Vibrational Properties of Liquid Water from van der Waals Density Functionals. *J. Chem. Theory Comput.* **7**, 3054-3061 (2011).
- 55 Li, Y. *et al.* Water-ion permselectivity of narrow-diameter carbon nanotubes. *Sci. Adv.* **6**, eaba9966 (2020).

Methods

Typical polymerization conditions

In a 20 mL reaction vial, 2-alkoxyisophthalic acid (**1a** - **1b**, 0.118 mmol) and 4,6-bis(octyloxy)isophthalohydrazide (**2**, 0.118 mmol) were introduced. Coupling reagents (0.354 mmol) were added to each reaction vial. This was followed by adding freshly distilled CH₂Cl₂ (5 mL) and 1 mL DMF (dimethylformamide) in a N₂ atmosphere. 100 μ L DIEA (N,N-Diisopropyl ethylamine) was then added in the reaction mixture, and the solution was stirred for 2 days at room temperature. After completion of reaction, solvent was evaporated to remove CH₂Cl₂ and DMF. The obtained residue was first washed with 10 mL MeOH/H₂O (1:1) and subsequently washed with 10 mL water and 10 mL MeOH and dried in oven (60 °C) to obtain polymers **3-5** as off-white solid powder with yields of 60 - 80%. Average molecular weights (M_n) of all these polymers were determined by Gel Permeation Chromatography.

Water transport and salt rejection study using a stopped-flow instrument

1,2-dioleoyl-sn-glycero-3-phosphocholine (DOPC, 0.24 mL, 25 mg/mL in CHCl₃, Avanti Polar Lipids, USA) and channel samples (**3** - **5** with and without LA or gA in chloroform) were mixed at different lipid to channel molar ratios (1500:1 to 9000:1) in micro-tubes (2 mL). The solvent was removed by N₂ flow and the resulting film was dried under high vacuum overnight. HEPES buffer (10 mM HEPES, 100 mM NaCl, pH = 7.0, 1.0 mL) was then added, followed by vortexing the solution for 30 s and then ten cycles of sonication (37 kHz, power 100, 70 °C, 2.5 min) in order to maximize incorporation extent of channel molecules into membrane. A glass spatula was used if necessary to make sure the residue was fully detached from the surface of the micro-tube. The mixture was further subjected to 10 freeze-thaw cycles (freezing in liquid N₂ for 1 min and heating 55 °C water bath for 2 min), and extruded at 80 °C for 15 times. The LUVs obtained this way contained 6 mg/mL of lipids and were stored in a 4 °C fridge before use, and diluted six times with HEPES buffer to make 1 mg/mL LUV for stopped flow measurements. The particle size of LUV (120 nm) was characterized by dynamic light scattering (Zetasizer Nano, Malvern Instruments Ltd., UK). The water permeability measurements were conducted on a stopped-flow instrument (Chirascan Circular Dichroism Spectrometer, Applied Photophysics, UK). Exposure of vesicles to three types of hypertonic osmolytes

resulted in the shrinkage of the vesicles due to an outwardly directed osmotic gradient. The abrupt decrease of the vesicle size leads to an increase in light scattering intensity at 90° angle based on the Rayleigh-Gans theory. The changes of light scattering intensity caused by vesicle shrinkage were recorded at a wavelength of 577 nm, and were fitted in the following form of single exponential function.

$$y = A * \exp(-kx) + y_0$$

where y = change in the light scattering, k is the exponential coefficient of the change in the light scattering and x is time.

With the assumption that change in the light scattering intensity is proportional to the change in the vesicle volume ($\Delta V/V_0$) based on the Boyle-van't Hoff law, the osmotic permeability (P_f) in the unit of cm/s was calculated as follow:

$$P_f = k / ((S/V_0) * V_w \times \Delta_{osm})$$

where k is the exponential coefficient of the change in the light scattering; S and V_0 are the initial surface area and volume of the vesicles, respectively; V_w is the molar volume of water, and Δ_{osm} is the osmolarity difference.

To calculate the true water permeability (P_{sc} in the unit of cm³/s) of water channels, the $P_{f(blank)}$ value of the blank vesicle without water channels needs to be deducted from $P_{f(channel)}$, which was multiplied by the vesical surface area (S) and divided by the number of water channels (N) incorporated in the liposome as shown below.

$$P_{sc} = (P_{f(channel)} - P_{f(blank)}) * (S/N)$$

The ability of **4-LA** to reject salts was first evaluated by comparing osmotic water permeability (P_f in cm/s) values under three hypertonic buffer solutions (300 mM sucrose, 150 mM NaCl or 150 mM KCl, Supplementary Fig. 6).

Determination of channel insertion efficiency

In order to calculate channel insertion efficiency of the water channels in the lipid bilayer membrane, a calibration curve was first created. At first, blank LUVs (without any synthetic channels) were prepared from 3 mg/mL to 7 mg/mL concentration by using the film rehydration method (without extrusion) as discussed above. All these solutions were scanned on a UV-Vis spectrometer and UV absorbance was found to be decreased proportionally with decrease in concentration. Calibration curve was plotted using this UV-Vis data at 280 nm. Blank LUVs were also prepared by extruding through 200 nm membrane for 15 times to obtain monodispersed unilamellar vesicles with an initial concentration of 6 mg/mL which is equivalent to our experimental condition. UV absorbance was recorded with these extruded blank liposomes at 280 nm wavelength. The obtained data was used to get actual lipid concentration *i.e.* 4.4 ± 0.7 mg/mL and around 20% lipid was lost during extrusion process.

Since the concentration of synthetic water channels is extremely low as compared to lipid concentration in our experimental condition, the UV-absorbance plots of lipid were found to be superimposed with the absorbance values of channels. Therefore, we measured fluorescence spectra of channel-containing liposomes ($\lambda_{ex} = 310$ nm, $\lambda_{em} = 430$ nm for channel molecules). In these experiments, two separate batches of liposomes, embedded with AWCs were prepared using film rehydration method as discussed earlier for each concentration ratio. One of the batches were not extruded and other batch was extruded through 200 nm membrane for 15 times to obtain monodispersed LUVs. Fluorescence spectra were recorded for all these channel-containing liposomes. Considering the lipid loss from the UV-Vis experiment and the ratio between fluorescence intensities (at $\lambda_{em} = 430$ nm) of non-extruded and extruded liposomes provided us the value of insertion efficiency of the AWCs in the lipid membrane. The obtained insertion efficiency values were further used to calculate actual single channel water permeability of AWCs.

Activation energy measurements

To determine activation energies for water transport, water transport kinetics was measured by using stopped-flow instrument from 6 °C to 25 °C. For these

experiments, temperature of the solution reservoir and the measurement cell of the stopped-flow instrument were maintained by a recirculating heater/chiller (Polystat, Cole Parmer). Light scattering kinetic rates representing water transport through AWCs at varying temperatures were fitted into the following Arrhenius equation to obtain activation energy (E_a).

$$\ln(k) = \ln(A) - E_a / (R * T)$$

where k is the exponential coefficient of the change in the light scattering; A is pre-exponential factor; E_a is activation energy; R is gas constant; T is absolute temperature.

Chloride ion permeability measurement

Cl⁻ ion permeability was measured using stopped-flow fluorescence analysis, with lucigenin dyes as molecular sensing probes. The transport rate obtained from these analyses was used to represent net monovalent ion (e.g., Na⁺ and Cl⁻) permeability of the channels. This method gives a conservative estimate of the monovalent ion permeability because, in actual desalination processes, Cl⁻ permeation is up to three orders of magnitude lower, as it is limited by the lower Na⁺ ion permeability and the condition of electroneutrality. Therefore, many analytical studies have adopted Na⁺ ions as a model molecule to analyse desalination processes. DOPC and **3-LA** reconstituted DOPC liposomes were prepared using the same method of preparing the samples for water permeability measurements except for that different rehydration buffer composition was used (1 mM lucigenin, 10 mM HEPES, 200 mM KNO₃, 10 μM valinomycin at pH 7.0). K⁺ ionophore valinomycin was added to mitigate the electrostatic imbalance caused by Cl⁻ permeation. After extrusion, the reconstituted vesicles were purified by Sephadex G-50 columns to remove free (unencapsulated) lucigenin dyes. The vesicles were exposed to the Cl⁻-containing buffer in the stopped-flow equipment, and quantitative Cl⁻ flux was calculated by the Stern-Volmer equation as shown in the following.

$$\frac{F}{F_0} - 1 = K_{sv} [Cl^-]$$

where F is fluorescence intensity change inside the vesicles over time, F_0 is the initial fluorescence intensity at Cl⁻ free condition which correspond to the initial ($t = 0$) fluorescence intensity from the stopped-flow experiments, $[Cl^-]$ is the molar concentration of the chloride inside the vesicles, and K_{sv} is the dye Stern-Volmer constant. The K_{sv} of the dye sensor within DOPC vesicles was experimentally determined as shown in Supplementary Fig. 13b. Permeability calculation was performed by utilizing the first derivative of the Stern-Volmer equation with respect to time (at times approaching zero) as shown below.

$$\left. \frac{d[Cl^-]}{dt} \right|_{t=0} = \frac{-1}{K_{sv} F_0} \left. \frac{dF}{dt} \right|_{t=0}$$

From the left side of the equation, quantitative Cl⁻ concentration change was calculated and influx of Cl⁻ through the vesicular membranes were calculated based on the size of the vesicles. The measurements were repeated at different concentration gradient conditions and the permeability coefficients were calculated from these data set.

Fluorescence correlation spectroscopy (FCS) to determine channel density of 3-LA in lipid membranes for the calculation of single channel Cl⁻ permeability

3-LA channels were labeled with 5-(and-6-)-((N-(5-aminopentyl)amino)carbonyl)tetramethylrhodamine fluorescence dyes using dicyclohexylcarbodiimide crosslinkers, by mixing the channels, dyes, and crosslinkers at a molar ratio of 1:10:10 in dimethyl sulfoxide (DMSO) for 24 hours at room temperature using a previously used procedure (REF). Unreacted free dyes were removed by dialysis with fresh DMSO. These dye-labeled channels were then used to prepare the **3-LA** reconstituted DOPC vesicles, and these vesicles were subjected to FCS experiments. The time dependent fluorescence fluctuation

inside the confocal volume was monitored using a Zeiss Laser Scanning Confocal microscope (LSM 880) 880 equipped with the Airyscan detector. A DPSS laser with an excitation wavelength at 561 nm, 20 mW was conducted to measure the emission intensity in the wavelength range from 570 nm to 695 nm. The average number of vesicles and micelles was measured for 10 seconds, obtaining 10 counts and through 3 repeated FCS measurements. The collected autocorrelation curves, $G(\tau)$, were fitted with the triplet state and translation parameters using the ZEN software (black edition).

$$G(\tau) = \frac{1}{N} \sum_{i=0}^M f_i \left[\frac{1}{1 + \tau/\tau_{D_i}} \right] \left[\frac{1}{1 + (r/z)^2 (\tau/\tau_{D_i})} \right]^{1/2}$$

where τ is the lag time, r and z are the radius and the half height of the confocal space, τ_{D_i} is the lateral diffusion time of fluorescence species i , and the N is the average number of fluorescence species in the confocal space. From this function, the number of 3-LA reconstituted vesicles were extracted (N_{ves}). After that, the same vesicle samples were completely micellized by adding a final concentration of 4 % (w/v) octyl β -d-glucoside (OG) and the sample analysis was repeated to obtain the average number of micellized channels ($N_{channel}$). From the ratio of $N_{channel}$ to N_{ves} , the channel number density in the DOPC vesicular membranes were determined (Supplementary Fig. 13c).

The HPTS assay for cation transport study under high salt gradient

30 μ L of HPTS-containing LUVs (please check supplementary information for detail protocol) was added to 1970 μ L of HEPES buffer (10 mM HEPES, 200 mM M_2SO_4 , pH = 8.0 where $M^+ = Na^+$ and K^+) in a clean fluorescence cuvette to generate a salt gradient across lipid bilayer. This cuvette was placed on the fluorescence instrument (at $t = 0$ s) equipped with magnetic stirrer. Fluorescence emission intensity of HPTS dye, F_t was monitored at $\lambda_{em} = 510$ nm ($\lambda_{ex} = 450$ nm) with time. Channels of various types (1 μ M, dissolved in DMF) was added at $t = 70$ s and recorded simultaneously for 300 seconds using fluorescence spectrophotometer (Hitachi, Model F-7100, Japan). Finally at $t = 370$ s, 20 μ L of 20% Triton X-100 was added to destroy all vesicles which resulted in destruction of pH gradient to achieve the maximum change in fluorescence emission intensity of HPTS dye. Fluorescence data was also recorded for gramicidin A (gA, 2 μ M) under same experimental condition and the obtained activity was compared with AWCs.

The time axis was offset according to the following equation: $t = t - 70$. Fluorescence intensities (F_t) were normalized to fractional emission intensity I_F using following equation:

$$I_F = [(F_t - F_0)/(F_\infty - F_0)] \times 100$$

whereas F_0 = Fluorescence intensity just before the compound addition (at $t = 0$ s), F_∞ = Fluorescence intensity at saturation after complete leakage (at $t = 300$ s), and F_t = Fluorescence intensity at time t .

The HPTS assay for anion and proton transport study

30 μ L of HPTS-containing LUVs (please check supplementary information for detail protocol) was added to 1970 μ L of HEPES buffer (10 mM HEPES, 67 mM K_2SO_4 , pH = 8.0) in a clean fluorescence cuvette to generate salt gradient across lipid bilayer. This cuvette was placed on the fluorescence instrument (at $t = 0$ s) equipped with magnetic stirrer. Fluorescence emission intensity of HPTS dye, F_t was monitored at $\lambda_{em} = 510$ nm ($\lambda_{ex} = 450$ nm) with time. Channels (3, 4, 5 and L8) or proton carrier (FCCP) at desired concentration in DMF was added at $t = 70$ s and recorded simultaneously for 300 seconds using fluorescence spectrophotometer (Hitachi, Model F-7100, Japan). Finally at $t = 370$ s, 20 μ L of 20% Triton X-100 was added to destroy all vesicles which resulted in destruction of pH gradient to achieve the maximum change in fluorescence emission intensity of HPTS dye. Exchange via H^+/M^+ antiport mechanism was monitored by change of fluorescence intensity of the HPTS dyes in presence of high salt gradient (200 mM Na_2SO_4 or K_2SO_4).

The time axis was offset according to the following equation: $t = t - 70$. Fluorescence intensities (F_t) were normalized to fractional emission intensity I_F using following equation:

$$I_F = [(F_t - F_0)/(F_\infty - F_0)] \times 100$$

whereas F_0 = Fluorescence intensity just before the compound addition (at $t = 0$ s), F_∞ = Fluorescence intensity at saturation after complete leakage (at $t = 300$ s), and F_t = Fluorescence intensity at time t .

The SPQ assay for anion transport activity study

The SPQ-containing LUV suspension (30 μ L, 10 mM in 225 mM $NaNO_3$) was added to a NaCl solution (1.7 mL, 225 mM) to create an extravascular chloride gradient. A solution of channel molecule 3-LA, 4-LA and 5-LA (1 μ M) or anion channel L8 (6 μ M) in DMF at different concentrations was then injected into the suspension under gentle stirring. Upon the addition of channels, the emission of SPQ was immediately monitored at 430 nm with excitations at 360 nm for 300 seconds using fluorescence spectrophotometer (Hitachi, Model F-7100, Japan) after which time an aqueous solution of Triton X-100 (20 μ L, 20% v/v) was immediately added to completely destruct the chloride gradient. The final transport trace was obtained by normalizing the fluorescence intensity using the following equation:

$$I_F = [(F_t - F_0)/(F_\infty - F_0)]$$

Where F_0 = Fluorescence intensity just before the compound addition (at $t = 0$ s), F_t = Fluorescence intensity at time t , and F_∞ = Fluorescence intensity at saturation after complete leakage (at $t = 300$ s).

Molecular dynamics simulations

All MD simulations were performed using the MD program NAMD⁵⁶, periodic boundary conditions and particle mesh Ewald (PME) method to calculate the long range electrostatics⁵⁷. The Nose-Hoover Langevin piston^{58,59} and Langevin thermostat⁶⁰ were used to maintain the constant pressure and temperature in the system. CHARMM36 force field parameters⁶¹ described the bonded and non-bonded interactions of among, lipid bilayer membranes, water and ions. A 8-10-12 \AA cutoff scheme was used to calculate van der Waals and short range electrostatics forces. All simulations were performed using a 2 fs time step to integrate the equation of motion. SETTLE algorithm⁶² was applied to keep water molecules rigid whereas RATTLE algorithm⁶³ constrained all other covalent bonds involving hydrogen atoms. The coordinates of the system were saved at an interval of 19.2 ps. The analysis and post processing the simulation trajectories were performed using VMD⁶⁴ and CPPTRAJ⁶⁵.

To build the initial PDB structures of LA-modified channels 3-5 of 2.9 nm in height, each having 26 repeating units 1 and 25 repeating units 2, quantum mechanics at the level of ω B97X/6-31G(d) was used to optimize symmetric short pore scaffolds consisting of four repeating units 1 and five repeating units 2 (Fig. 1b) that were created using Gaussview⁶⁶. Based on these QM-derived structures, which look nearly identical to their respective crystal structures in Supplementary Fig. 1b in terms of bond angle and cavity enclosed, longer channels, i.e., LA-modified channels 3-5, were built using Gaussview and then subjected to MD simulation. The topology and force field parameters for the monomeric unit of the channel (along with all three variant 3, 4, 5) and LA anchor were obtained using the CHARMM general force fields (CGenFF) webserver.⁶⁷ We connected the LA anchors to the terminal residues and obtained the protein structure file (psf) of the channels using the psfgen tool of VMD. The channels were then embedded into a 9×9 nm² patch of pre-equilibrated POPC lipid bilayer membrane. The lipid patch was generated using the CHARMM-GUI membrane builder⁶⁸ and pre-equilibrated for approximately 400 ns. Lipid molecules that overlapped with the channel were removed. The system was then solvated with water⁶⁹ using the Solvate plugin of VMD. Sodium and chloride ions were added to 1 M concentration using the Autoionize plugin of VMD. The final assembled system measured $9 \times 9 \times 9$ nm³ and contained approximately 80,000 atoms.

Following the assembly, the system underwent 1200 steps of energy minimization using the conjugate gradient method to remove steric clashes. After energy minimization, the system was subjected to a 50 ns equilibration at a constant number of atoms (N), pressure (P = 1 bar) and temperature (T = 300 K), the NPT ensemble, with harmonic restraints applied to all non-hydrogen atoms of channels that surrounded the transmembrane pore. The restraints were applied relative to the initial coordinates of the atoms, the spring constants were 1 kcal mol⁻¹ Å⁻². After 50 ns, the harmonic restraints were removed, and the system was equilibrated free of any restraints for ~700 ns.

The initial all-atom model of AQP embedded in a lipid membrane was taken from a previous study⁷⁰ and simulated using the protocols described above.

Reporting summary

Further information on research design is available in the Nature Research Reporting Summary linked to this paper.

Data availability

The datasets that support the finding of this study are available in figshare repository with the identifier(s) (<https://figshare.com/s/0354959049b2c0ed4c61>)

References

- Phillips, J. C. *et al.* Scalable molecular dynamics with NAMD. *J. Comp. Chem.* **26**, 1781-1802 (2005).
- Darden, T., York, D. & Pedersen, L. Particle mesh ewald - An N.log(N) method for ewald sums in large systems. *J. Chem. Phys.* **98**, 10089-10092 (1993).
- Feller, S. E., Zhang, Y., Pastor, R. W. & Brooks, B. R. Constant pressure molecular dynamics simulation: the Langevin piston method. *J. Chem. Phys.* **103**, 4613-4621 (1995).
- Martyna, G. J., Tobias, D. J. & Klein, M. L. Constant pressure molecular dynamics algorithms. *J. Chem. Phys.* **101**, 4177-4189 (1994).
- Sindhikara, D. J., Kim, S., Voter, A. F. & Roitberg, A. E. Bad seeds sprout perilous dynamics: Stochastic thermostat induced trajectory synchronization in biomolecules. *J. Chem. Theor. Comp.* **5**, 1624-1631 (2009).
- Klauda, J. B. *et al.* Update of the CHARMM all-atom additive force field for lipids: validation on six lipid types. *J. Chem. Phys.* **114**, 7830-7843 (2010).
- Miyamoto, S. & Kollman, P. A. Settle: An analytical version of the SHAKE and RATTLE algorithm for rigid water models. *J. Comp. Chem.* **13**, 952-962 (1992).
- Andersen, H. C. Rattle: A "velocity" version of the shake algorithm for molecular dynamics calculations. *J. Comp. Chem.* **52**, 24-34 (1983).
- Humphrey, W., Dalke, A. & Schulten, K. VMD: Visual molecular dynamics. *J. Mol. Graph.* **14**, 33-38 (1996).
- Roe, D. R. & Cheatham, T. E., III. PTRAJ and CPPTRAJ: Software for Processing and Analysis of Molecular Dynamics Trajectory Data. *J. Chem. Theor. Comp.* **9**, 3084-3095 (2013).
- Gaussian 16 Rev. C.01 (Wallingford, CT, 2016).
- Vanommeslaeghe, K. *et al.* CHARMM general force field: A force field for drug-like molecules compatible with the CHARMM all-atom additive biological force fields. *J. Comp. Chem.* **31**, 671-690 (2010).
- Jo, S., Kim, T., Iyer, V. G. & Im, W. CHARMM-GUI: a web-based graphical user interface for CHARMM. *J. Comp. Chem.* **29**, 1859-1865 (2008).
- Jorgensen, W. L., Chandrasekhar, J., Madura, J. D., Impey, R. W. & Klein, M. L. Comparison of simple potential function for simulating liquid water. *J. Chem. Phys.* **79**, 926-935 (1983).
- Decker, K. *et al.* Selective Permeability of Truncated Aquaporin 1 in Silico. *ACS Biomater. Sci. Eng.* **3**, 342-348 (2017).

Acknowledgements This study was supported by Institute of Advanced Synthesis, Northwestern Polytechnical University, China, NanoBio Lab (Biomedical Research Council, Agency for Science, Technology and Research, Singapore), the Singapore National Research Foundation under its Environment and Water Research Programme and administered by PUB, the National Science Foundation (USA) under grant DMR-1827346, the National Institutes of Health under grant P41-GM104601. The work in MK lab was supported by the US National Science Foundation under grants CBET 1946392 and CBET 1952295. Supercomputer time was provided through the Early Allocation grant on Frontera (FTA-Chemla), XSEDE Allocation Grant no. MCA05S028 and the Blue Waters petascale supercomputer system at the University of Illinois at Urbana-Champaign.

Author contributions A.R. synthesized polymers **3** and **5** and conducted water/ion transport study; J.S. synthesized polymers **4** and conducted water/ion transport study; H.J. and A.A. performed MD study; W.S., Y.T. and M.K. determined water over chloride selectivity and proton transport rates; RC and MK conducted analysis of proton exclusion simulations; R.Y., N.L. and C.R. performed some ion transport study; H.Z. conceived the project and wrote the manuscript with input from A.R. and M.K.. All authors edited the manuscript.

Competing interests The authors declare no competing interests.

Additional information

Supplementary information is available for this paper at <https://doi.org/xxxxxx>.

Correspondence and requests for materials should be addressed to H.Z.

Reprints and permissions information is available at <http://www.nature.com/reprints>.

Figure Legends

Figure 1: Molecular design and synthetic construction of foldamer-derived polymer-based synthetic water channels. **a**, Chemical structures of artificial water channels **3** – **5**, which have inwardly facing methyl- (**3**), ethyl- (**4**), or isopropyl- (**5**) aliphatic groups for tuning the inner-pore size and hydrophobicity, respectively. **b**, QM-optimized backbone scaffolds of **3** – **5**, illustrating excellent structural correspondence to the crystallographic structures of methyl- and ethyl- containing trimeric repeating units (See **6a** and **6b** in Supplementary Fig. 1b for details). **c**, Cross-sections of MD snapshots of water-filled lipid anchor-containing channels **3** and **4**, each containing 26 units of **1** and 25 units of **2** and having a height of 2.9 nm, in POPC membrane. The system is solvated in 1 M NaCl, with the volume occupied by the electrolyte solution represented as semi-transparent surfaces. POPC = (1-palmitoyl-2-oleoyl-sn-glycero-3-phosphatidyl choline).

Figure 2: Selective water permeation through foldamer-based polymeric AWCs. **a**, Chemical structures of lipid anchor (LA)-modified AWCs. **b**, Representative stopped-flow light scattering traces of **3** and **3-LA** reconstituted DOPC vesicles under the inwardly directed osmotic gradients. **c**, Single channel permeability of channels before and after LA modification. **d** and **e**, Schematic illustrations of HPTS-based fluorescence assays, demonstrating high rejection of (**d**) cations (Na⁺ or K⁺) and (**e**) anion (Cl⁻) and proton through the channels. **f**, Stopped-flow fluorescence traces of **3-LA** reconstituted DOPC vesicles, encapsulating lucigenin dyes for sensing Cl⁻ permeation that is driven by inwardly directed Cl⁻ concentration gradients (20 mM). **g**, Plots of Cl⁻ permeation flux as a function of Cl⁻ concentration gradients for both DOPC and **3-LA** reconstituted DOPC membranes. **h**, Comparison of water-to-salt permselectivity of **3-LA** to the values of several representative water channels and current polymeric desalination membranes. Intrinsic water-to-salt selectivity (P_w/P_s) vs water permeability (P_w , cm²/s) plot. P_w/P_s vs P_w values for **3-LA** reconstituted biomimetic membranes in a DOPC matrix, which were compared with other representative water channels, AQP1 and CNTPs with pore diameter of ~0.47 nm^{13,34}. The α values in the plot indicate the fractional volume of the biomimetic membranes occupied by water channels (e.g., $\alpha = 0.5$ represents the membranes of which the half volume is composed of the channels). Dashed line is the current polymer desalination membranes' permeability-selectivity upper bound limit^{10,12}. Data in c), f) and g) are the average of three independent measurements with error bars representing the standard deviations.

Figure 3: MD simulations of water transport and the mechanism of proton rejection by proton wire breakers created due to the presence of fluctuating alkyl groups. **a**, Number of water molecules observed to pass through LA-containing **3** - **5** and AQP1 in equilibrium MD simulations. The channel structure was harmonically restrained for the first 50 ns. **b**, Number of water molecules inside the pores of channels **3-LA** and **4-LA**. **c**, Illustration of proton transport through an ideal proton wire via the Grothuss mechanism. **d**, Irregularly H-bonded water molecules, serving as proton wire breakers to block proton transport via the Grothuss mechanism. **e**, Fractions of proton wire breakers over all water molecules inside **3-LA** and **4-LA**. **f**, Inward protrusions of Me and Et groups transiently reduce local cross section of channels **3-LA** and **4-LA**. **g**, Breakage of proton water wire caused by protrusion of Me (left) and Et (right) groups.

Table 1. Computed number of intermolecular H-bonds per water molecule formed among water molecules in the channel, and between water molecule and channel's inner wall^a

	3-LA	4-LA	AQP1
Water-Water	2.0 (± 0.2)	1.9 (± 0.3)	1.6 (± 0.1)
Water-Wall	0.8 (± 0.1)	0.8 (± 0.1)	1.6 (± 0.1)
Total	2.8 (± 0.3)	2.7 (± 0.4)	3.2 (± 0.2)

^a Average values and standard deviations in H-bond were computed for the whole simulation trajectory after excluding the first 50 ns of the simulation where the channels were harmonically restrained (Supplementary Fig. 19a-c).